Oral presentation | Turbulence simulation (DNS,LES,RANS)
Turbulence simulation(DNS,LES,RANS)-IV
Thu. Jul 18, 2024 2:00 PM - 4:00 PM Room B

[11-B-02] Hybrid RANS-LES Method for Simulating an Installed Rotor in Hover and Descent Flight

*Chunhua Sheng[1] （1. The University of Toledo, Ohio, USA）

Keywords: Hybrid Method, Mesh Deformation and Motion, Rotorcraft

Twelfth International Conference on Computational Fluid Dynamics (ICCFD12)
Kobe, Japan, July 14-19, 2024

Hybrid RANS-LES Method for Simulating an Installed Rotor in Hover and Descent Flight

Chunhua Sheng and Qiuying Zhao
Corresponding author: chunhua.sheng@utoledo.edu
The University of Toledo, Ohio, USA.

Abstract: This study presents computational simulations of a Hover Validation and Acoustic Baseline rotor operating in both hover and descent flight conditions. A global hybrid simulation approach is employed, integrating the Reynolds-Averaged Navier-Stokes (RANS) turbulence model with a Large Eddy Simulation (LES) subgrid model to enhance turbulence prediction accuracy. Three key elements of this hybrid simulation strategy are highlighted: the selection of a blending method for the RANS and LES models, a high-order numerical scheme, and multibody relative grid motion and deformation to facilitate the simulation of an installed rotor. These techniques enable detailed and flexible rotor blade motions, accommodating the complex geometries and flow dynamics of rotorcraft in various flight condition.

Keywords: Hybrid Method, Mesh Motion and Deformation, Rotorcraft.

1 Introduction

Computational simulations of rotorcraft aerodynamics encounter two significant challenges. The primary hurdle involves accurately modeling the intricate motion of rotor blades during various flight conditions, including hover, forward flight, and transient maneuvers. Rotor blades exhibit elastic properties, particularly in conventional rotors, and their motions are influenced by collective/cyclic pitch changes and aerodynamic forces. The second major challenge is to effectively capture the complex physics inherent in rotor flows. This includes phenomena such as trailing tip vortices, boundary layer transitions, and flow separations occurring on rotor blades. These dynamics play crucial roles in determining aerodynamic efficiency, noise generation, and overall performance of rotorcraft. Addressing these challenges is essential for advancing computational methods in rotorcraft aerodynamics, ensuring simulations provide accurate predictions that align with experimental data and enhance the design and optimization processes of rotor systems.

The present study presents a computational method to investigate a Hover Validation and Acoustic Baseline (HVAB) rotor [1] in hover and descent flight. The method is based a computational fluid dynamics (CFD) solver [2] using unstructured grid technologies. This study examines several critical aspects of rotor behavior, including overall hover performance, the complex flow fields over rotor surfaces, and the formation and evolution of trailing tip vortices in the rotor downwash. To achieve this, a hybrid Reynolds-Averaged Navier-Stokes (RANS) and Large Eddy Simulation (LES) approach is employed.

There are two major hybrid modeling strategies developed in recent years: the unified (global) model and the zonal (segregated) model [3]. The unified model blends the RANS and LES models using a different length scale, while in the zonal model, RANS and LES are treated separately and their respective turbulent eddy viscosities are combined. However, inconsistencies can arise at the RANS-LES interface in the zonal model, leading to issues such as log-layer mismatch, reduced mass flow rate, or even non-physical separation [4].

Significant advancements have been made in unified hybrid RANS-LES modeling, notably Spalart's Detached Eddy Simulation (DES) [5] based on the Spalart-Allmaras (SA) model and Menter's Scale-Adaptive Simulation (SAS) [6] based on the Shear Stress Transport (SST) k-ω turbulence model. Spalart developed the DES model to address complex flows with massive separations, but the model may suffer from Modeled Stresses Depletion (MSD) due to under-resolved LES simulation [7]. To

mitigate this issue, Spalart, et al. introduced an improved version known as Delayed Detached-Eddy Simulation (DDES) [7].

The current hybrid strategy is built upon a unified global methodology that integrates RANS and LES models using a blending method [8]. An innovative aspect of this study is the implementation of an entropy-based blending function [9], which effectively distinguishes the RANS-dominated near-wall region from the LES-dominated off-wall region, thereby enhancing the accuracy of hybrid simulations. Furthermore, employing a high-order, low-dissipation numerical scheme is essential for resolving turbulence within the LES region. For this purpose, a new Weighted Essentially Non-Oscillatory (WENO) scheme [10] has been adopted in this study. This scheme significantly reduces numerical dissipation errors, allowing for the resolution of a substantial portion of the turbulent kinetic energy spectrum within the LES region. Additionally, advanced unstructured grid techniques, such as multibody relative motion and mesh deformation [11], have been utilized to model an installed rotor operating in hover and descent flight.

The subject of this study is a Hover Validation and Acoustic Baseline rotor [1] currently being tested by the NASA/US Army team at the National Full-Scale Aerodynamics Complex (NFAC) in their 80 ft by 120 ft test facility. It is a model-scale, four-bladed rotor with a radius of 66.5 inches. This rotor is mounted on a Robin-7 fuselage to account for rotor-airframe interactions. Operating at a rotational speed of 1250 RPM, the rotor achieves a tip Mach number of 0.65 under standard day sea level conditions. These wind tunnel experiments provide crucial performance data in validating the computational simulations using the current hybrid methodology.

2 Computational Method

The rotor simulations are performed using an unstructured node-based, high-fidelity, finite-volume computational fluid dynamics (CFD) solver [2]. This solver solves three-dimensional, unsteady Reynolds-Averaged Navier-Stokes (RANS) equations and Large Eddy Simulation (LES) model utilizing multi-element unstructured grids. It is specifically designed to handle realistic rotorcraft flows that involve complex geometries and intricate physics, especially in grids with relative motions. To achieve unsteady time-accurate solutions, the solver employs an implicit Newton's method. During each Newton iteration, symmetric Gauss-Seidel relaxations are used to solve the resulting linear system of equations.

2.1 Hybrid RANS-LES Methodology

The current simulations use a hybrid methodology that integrates the Spalart-Allmaras (SA) turbulence model [11] with the Wall-Adaptive Local Eddy viscosity (WALE) subgrid model [13]. The Spalart-Allmaras turbulence model is based on a single transport equation for effective viscosity $\tilde{\nu}$, allowing the computation of turbulent eddy viscosity ν_t. The subgrid scale model used here is the WALE model [13], which does not require secondary filtering.

A simple way to combine the LES and RANS models into a hybrid model is to apply a blending function. The blending function, F_B, is a continuous function in space and time that is calibrated empirically. The factors F_B and $(1 - F_B)$ constitute a partition of unity since they add up to one. The eddy viscosity of both models is blended using the following formula:

$$\nu_{ij} = \nu_{ijRANS} F_B - (1 - F_B)\nu_{ijLES} \tag{1}$$

It is crucial that the blending function remains at F_B = 1 inside boundary layers and F_B = 0 outside the boundary layer. This ensures that viscous flow inside the boundary layer can be solved using well-established turbulence models, such as the Spalart-Allmaras (SA) and Menter's Shear Stress Transport (SST) κ–ω model. Meanwhile, the flow outside the boundary layer in the off-wall region is resolved using the subgrid scale model, such as the WALE model. This ensures that both RANS and LES models are employed in the correct regions, yielding optimal results in the hybrid simulation.

The blending function initially designed to integrate the SA and WALE models was analogous to Spalart's Delayed Detached Eddy Simulation (DDES), as described in reference [8]:

$$F_2 = tanh[\left(c\frac{\max(\mu_t,\mu_l)}{\rho\kappa^2 d_w^2 S}\right)^n] \tag{2}$$

where κ is the von Karmen constant and S is the strain rate. μ_t and μ_l are the turbulent eddy viscosity and molecular viscosity. While this blending function worked reasonably well for simple viscous flows, such as those over a flat plate or stationary airfoil, it failed to properly distinguish the RANS and LES regions in more complex flows, as an installed rotor presented here. Figure 1 illustrates the RANS and LES regions determined by the F_2 blending function (2) for the HVAB rotor in ground effect. In the figure, the blue color represents the off-wall LES region, while the red color represents the near-wall RANS region. It shows that the RANS region extends far into the rotor wake region, resulting in under-resolved turbulence in critical rotor downwash flows.

To address this deficiency, a different blending function based on entropy production [9] is introduced here. Since the turbulent boundary layer accounts for at least two-thirds of the entropy production, this information can be utilized to distinguish the boundary layer from the rest of the flow. Zhou, et al. [9] proposed a Shielded Detached Eddy Simulation (SDES) based on entropy production to address the common "double-buffer problem" or "log-layer mismatch" in hybrid simulations. An entropy increment ratio $\bar{S}_{vis}^{\square}$, caused by viscous dissipation, is adopted to construct a blending function for the current hybrid simulation:

$$F_s = 1.0 - tanh\left(\frac{\bar{S}_{vis}^{\square}}{l_s^{3\square}}\right) \tag{3}$$

where $\bar{S}_{vis}^{\square}$is the ratio of the entropy increase relative to the maximum increase for a given flow. $l_s^{\square}$ is the length-scale ratio, which should be less than 1.0 in the boundary layer and increase quickly outside the boundary layer:

$$\bar{S}_{vis}^{\square} = \begin{cases} C_s f\frac{d_w}{C_{DES}}, & \text{if } \bar{S}_{vis}^{\square} > 0.05 \\ \frac{d_w}{C_{DES}}, & otherwise \end{cases}$$

where C_s= 0.12, C_{DES} = 0.65, d_w is a distance to the wall and f is a function of the grid cell skewness.

The application of entropy-based blending function (3) yields a smooth transition between the RANS and LES regions in the HVAB hybrid simulations, as illustrated in Figure 2 for the same HVAB rotor in ground effect. The new blending function effectively confines the RANS model to the near-body region of the rotorcraft and near the ground, while allocating the far-wall region to the LES model for enhanced viscous resolutions.

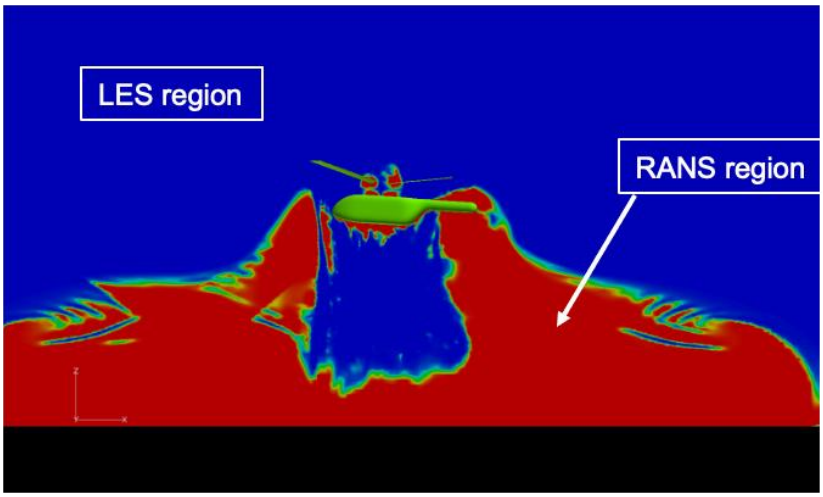

Figure 1. RANS and LES regions using original F_2 function for HVAB rotor IGE.

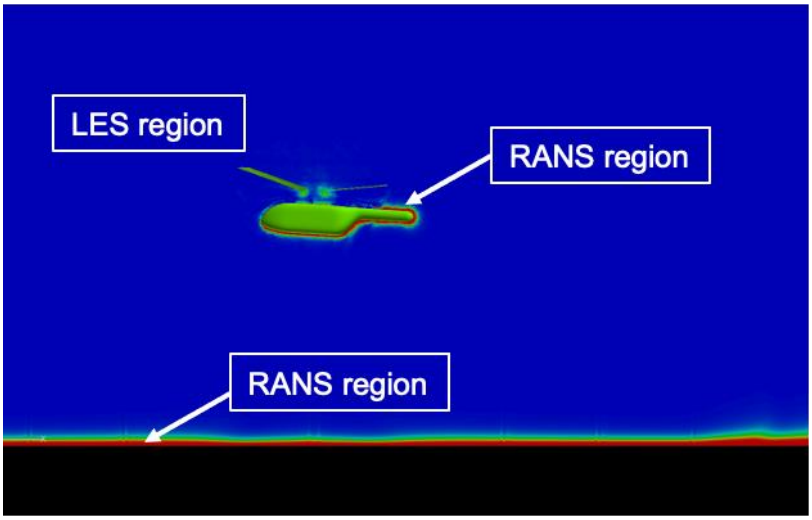

Figure 2. RANS and LES regions using new *Fs* function for HVAB rotor IGE.

2.2 High Order Compact WENO Schemes

The hybrid simulation combines the RANS model for near-wall viscous flow modeling and the LES model to resolve turbulence in off-wall regions like the rotor downwash wake. A critical requirement for this approach is the high-order scheme to minimize the numerical dissipation errors, enabling resolution of a majority of turbulent kinetic energy in LES. For this purpose, a high-order compact WENO scheme developed for unstructured grids [10] is employed for the HVAB rotor hybrid simulation. This high-order WENO scheme utilizes one large stencil in the smooth flow region and two small stencils in the discontinuous flow regions, providing guaranteed positive linear weights as detailed in [14]. The adaptive formula for the new WENO scheme is expressed as follows:

$$u^{\pm}(x) = \omega_3 \left(\frac{1}{\gamma_3} p_3(x) - \frac{\gamma_1}{\gamma_3} p_1(x) - \frac{\gamma_2}{\gamma_3} p_2(x) \right) + \omega_1 p_1(x) + \omega_2 p_2(x) \quad (4)$$

where $\gamma_1, \gamma_2, \gamma_3$ are the positive linear weights satisfying the condition $\gamma_1 + \gamma_2 + \gamma_3 = 1$ ($\gamma_3 \neq 0$). $\omega_1, \omega_2, \omega_3$ are the non-linear weights based on the linear weights and smoothness indicators. $p_1(x), p_2(x)$ are the two small stencils and $p_3(x)$ is the large stencil. $u^{\pm}(x)$ are the final reconstructed variables, representing the high-order approximations to the solution $u(x, \mathrm{t})$ on the face of the control volume scheme.

It is evident that as the scheme's order increases, a greater number of neighboring points is necessary to construct the stencil. This results in very large stencils for unstructured grid schemes, particularly for those using node-based data structures. To tackle this issue, a new strategy was introduced in [10] in constructing a compact WENO scheme on arbitrary grids. The central ideal involves computing these neighboring points using the first and second gradients of the two immediate points located on the left and right sides of the interface. By employing this strategy, a series of high-order compact WENO schemes have been developed [10]. Figure 3 displays the simulation results on tip vortices generated by a propeller using different unstructured compact WENO schemes. The results show that the sixth-order scheme (WENO6) captured the most vortex wake structures due to reduced dissipation errors. Therefore, this scheme is used in the current hybrid simulation for the HVAB rotor under various flight conditions.

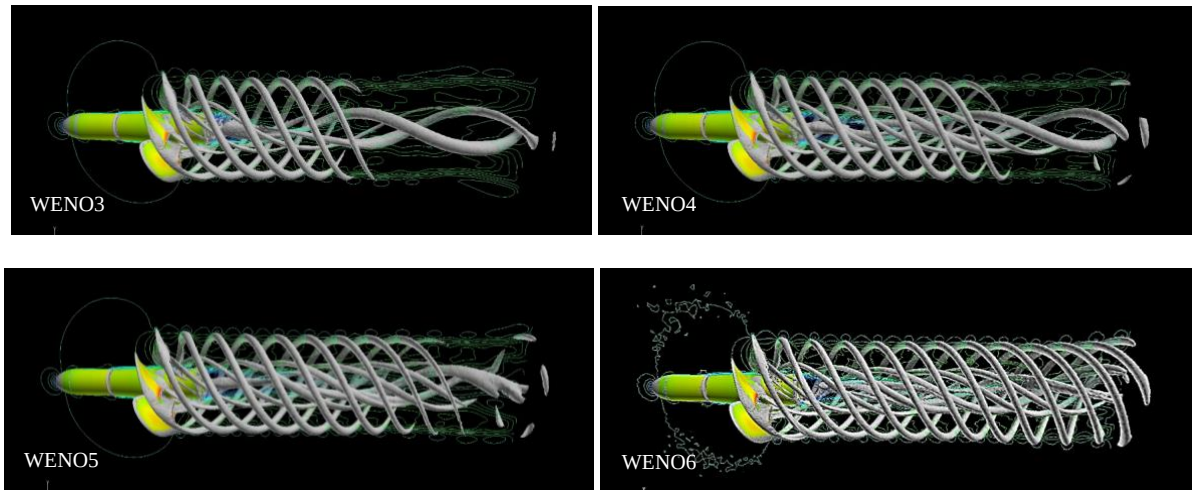

Figure 3. Simulation of a propeller using different WENO schemes.

2.3 Multi-Body Relative Motion and Deformation

To simulate an installed rotor during hover and descent flights, advanced unstructured grid techniques are utilized, including multi-body relative grid motion and deformation. This approach involves multiple volume grids to accommodate both rigid motion and/or flexible deformation of bodies. Key to this technology is a conservative non-interpolative method for data exchange among relative moving grids. This ensures that conservation laws are satisfied within each control volume cell, thereby maintaining continuous solutions across the interfaces of the relative motion grids. This technique is essential for accurately modeling the dynamics and interactions of the installed rotor in various flight scenarios.

Conventional helicopter blades are characterized by their length and flexibility, involving a combination of rigid motions (such as collective and cyclic pitch changes) and elastic deformations during operation. The intricate nature of rotor blade motions necessitates the use of a mesh deformation capability. The mesh deformation is typically employed in coupled CFD/CSD (Computational Fluid Dynamics/ Computational Structural Dynamics) simulations to analyze unsteady aeromechanics of rotorcraft [15]. In the present study, this technique is specifically applied to showcase its functionality in modeling a rotorcraft undergoing a descent maneuver flight.

The mesh deformation method employed is based on a radial basis function (RBF) [11]. The general form of the RBF method can be expressed as:

$$f(x) = \sum_{i=1}^{n} \lambda_i \phi(\|x - x_i\|) \tag{5}$$

Here, $r = \|x - x_i\|$) represents the distance between the point x and the basis point x_i, and λ_i is the weighting function. ϕ is the radial basis function.

Figure 4 depicts the multi-volume grid topology employed for simulating the installed HVAB rotor during descending flight. Each volume grid accommodates body's rigid and flexible motions separately or concurrently. While this method may not encompass all rotor flight motions, it only showcases its unique capability in simulating an installed rotor undergoing a complex maneuver flight. Detailed results will be presented in the subsequent section.

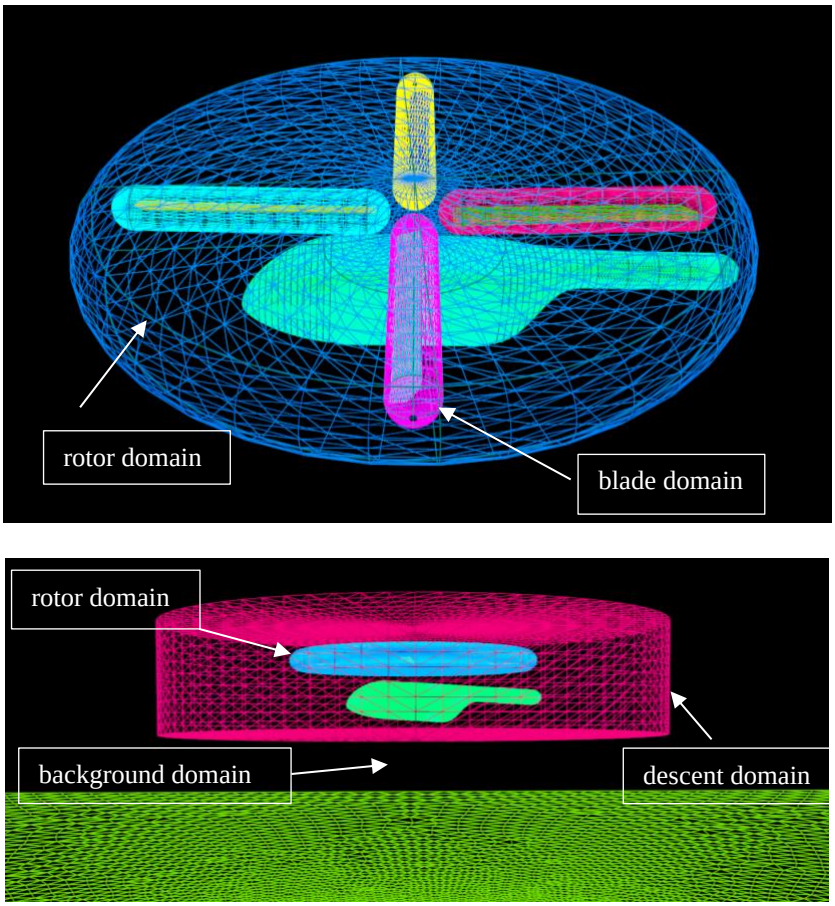

Figure 4. Grid topology for installed rotor undergoing descent flight.

3 Results

The Hover Validation and Acoustic Baseline (HVAB) rotor [1] investigated here is a four-bladed rotor with a radius of 66.5 inches. The blade properties such as swept tapered tip, twist, solidity, and tip chord length etc. are provided in Table 1. The rotor operates at 1250 RPM, corresponding to a tip Mach number of 0.65 under standard day sea level conditions. Figure 5 shows the blade platform featuring a distribution of RC-series airfoils. This setup is typical for studying rotor aerodynamics and performance characteristics in simulations and research.

Simulations are performed for the HVAB rotor at a tip Mach number of 0.65, with the blade collective pitch angle fixed at 10°. The collective angle and the corresponding coning and lag angles are built into aeroelastically deformed blades in the current simulations. The simulations are conducted using a minimum time step equivalent to one degree of rotor rotation per time step. To achieve fully converged rotor thrust and torque, the simulations are run for a total of 20 to 25 rotor revolutions in hover flight. The computational results are compared and validated with the available experimental data.

Table 1 HVAB Rotor Properties and Operating Conditions [1]

No. of Blades	4
Radius	66.5 in
Solidity	0.1033
Reference Chord	5.45 in
Tip Chord	3.27 in
Tip Sweep	30 deg. at 95% radius

Flap Hinge	3.0 in
Rotor Rotational Speed	1250 RPM
Tip Mach Number	0.65 at sea level standard (SLS)

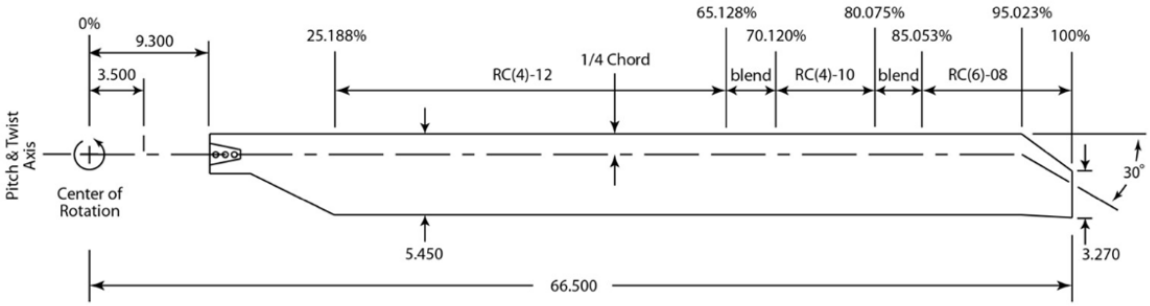

Figure 5. HVAB rotor platform [1]

3.1 HVAB Rotor in Hover

Two unstructured meshes are generated for simulating the HVAB rotor in hover: one for an isolated rotor and another for an installed rotor. The mesh sizes are approximately 35.86 million points for the isolated rotor and 33.12 million points for the installed rotor. Both meshes maintain the same surface grid resolution and a y+ value of one on all solid surfaces. Additionally, an interior surface is created along the rotor downwash region to help capture important rotor wake flows. Figure 6 illustrates the mesh resolutions for the isolated HVAB rotor from side and top views on two cutting planes. Meanwhile, Figure 7 depicts the mesh resolution for the installed rotor, focusing on the downwash region and the vicinity surrounding the rotor and airframe.

Computed rotor integrated thrust and power coefficients for both isolated and installed rotors are shown in Figs. 8 and 9, respectively, which are compared with the experimental data [1]. Additionally, results from a previous simulation for an isolated rotor using single blade model [16] are included here for reference. It should be noted that the previous single blade model featured a significantly higher rotor surface grid resolution, nearly six times more points compared to the current CFD mesh. This discrepancy accounts for slightly better figure of merit (FM) predicted in the previous simulation compared to the current simulation at the same pitch angle (10°). When comparing the current isolated and installed rotor cases, the rotor thrust shows a slight increase in the installed rotor configuration due to the fuselage to cause a ground effect. However, the rotor power consumption also increases due to the rotor and airframe interaction, resulting in a slightly decreased figure of merit (FM) compared to the isolated rotor configuration.

Figures 10 and 11 depict how the dimensional thrust and torque of the rotor change with varying blade pitch angles. These figures demonstrate that rotor thrust increases almost linearly with the blade collective pitch, showing an approximate rise of 100 lbf per degree of the blade pitch increment. In contrast, rotor torque shows an exponential growth with the blade pitch angle, especially at higher thrust levels. This is primarily attributed to deteriorating flow conditions, such as flow separations at the blade tips, which modifies the rotor aerodynamic load and power consumption.

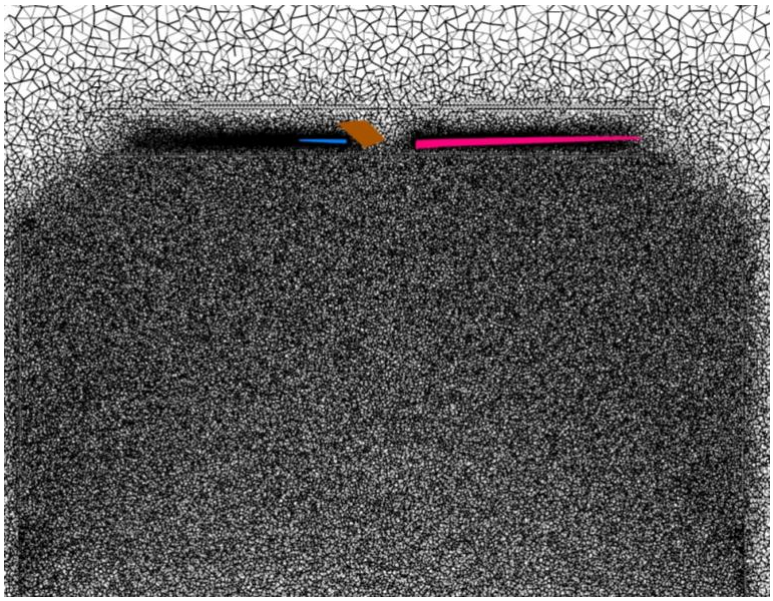

Figure 6(a). Side view of mesh resolution on a cutting plane for the isolated rotor.

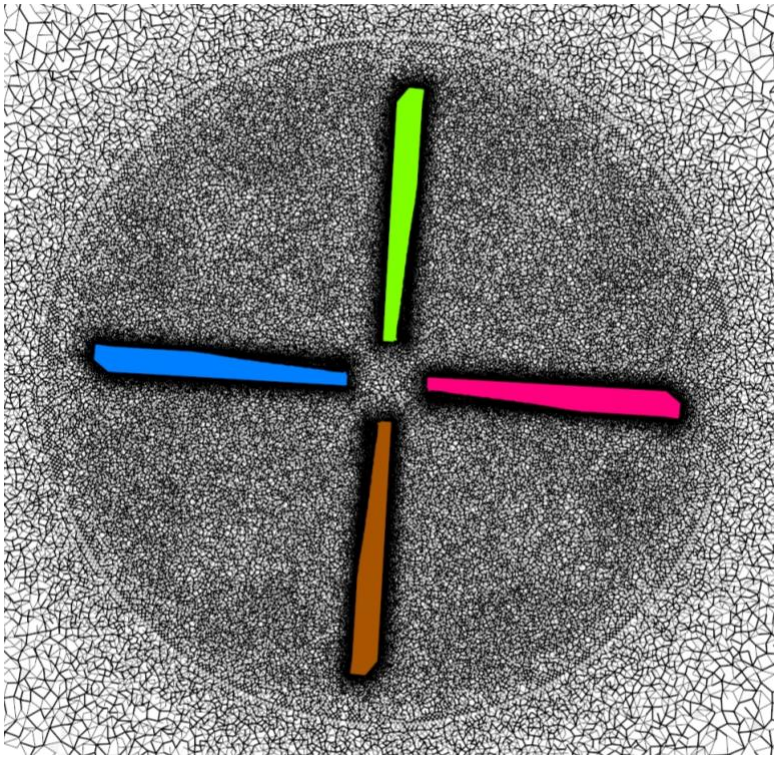

Figure 6(b). Top view of mesh resolution on a cutting plane for the isolated rotor.

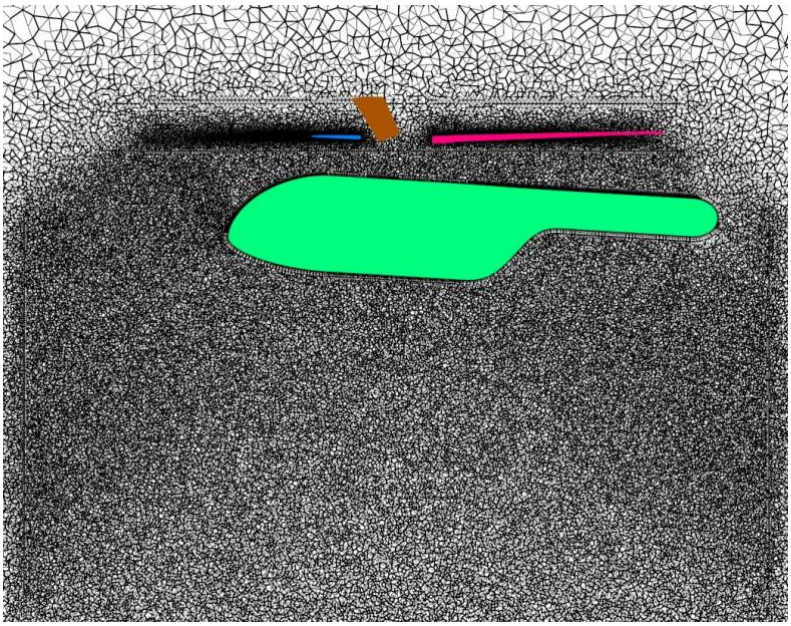

Figure 7(a). Side view of mesh resolution in the downwash of the installed rotor.

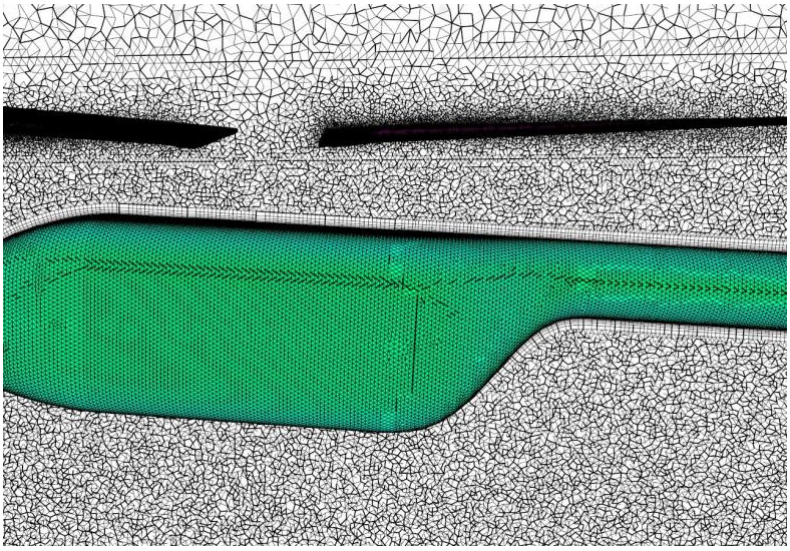

Figure 7(b). Close view of mesh resolution in the vicinity of the installed rotor.

In Table 2, the rotor thrust, torque, and figure of merit for both isolated rotor and installed rotor predicted at 10° blade pitch angle are listed, alongside wind tunnel test data measured under the same conditions. For installed rotor, the installed thrust (or torque) refers to the thrust (or torque) generated on the rotor when mounted on fuselage, while the net thrust (or torque) refers to the installed thrust (or torque) minus the download (or torque) generated on the fuselage. Computations show elevated rotor thrust and torque predicted for both isolated and installed rotors compared to the measured data. This discrepancy may be due to the blade pitch angle offset between the computation and experiment settings. Comparing the predictions between the isolated and installed rotors, the installed rotor generates 1.2% more installed thrust and 4.7% more installed torque compared to the isolated rotor, attributed to the fuselage interaction (e.g., ground effect). However, the installed rotor generates 3.6% less net thrust compared to the isolated rotor case, due to the download generated on fuselage. The aerodynamic interaction between the rotor and fuselage also causes a decrease of figure of merit, or efficiency for the installed rotor operating in hover.

Table 2 Comparison of rotor thrust, toque, and figure of merit at blade pitch angle of 10°.

	Installed Rotor (installed value)	Installed Rotor (net value)	Isolated Rotor	Exp. (natural & forced transition)
Thrust (lbf)	1020.2	968.8	1007.8	952.9 & 936.4
Torque (lbf-ft)	536.8	515.3	512.7	446.6 & 437.6
Figure of Merit	0.6846	0.6600	0.7037	0.7418 & 0.7422

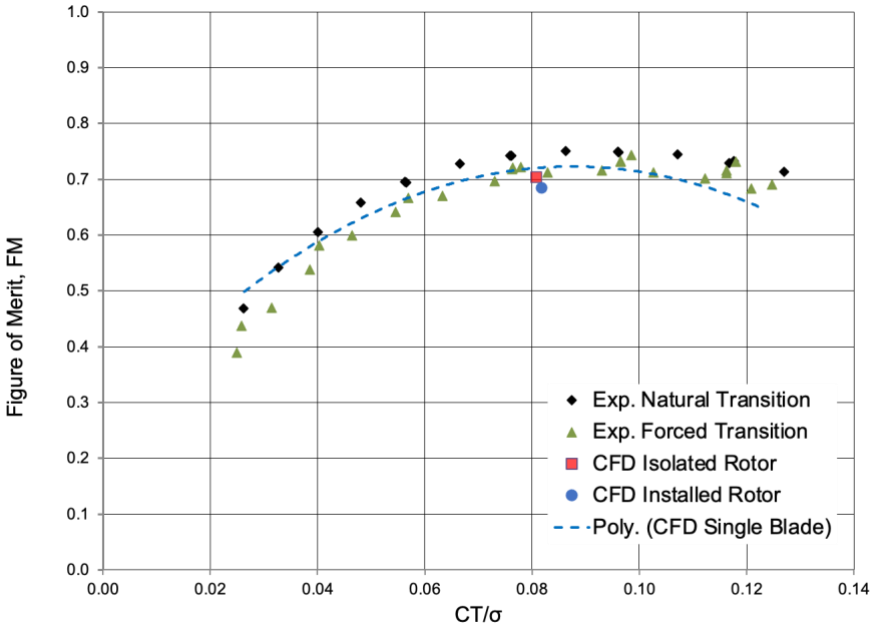

Figure 8. Comparison of FM vs. Ct/s for isolated and installed rotors.

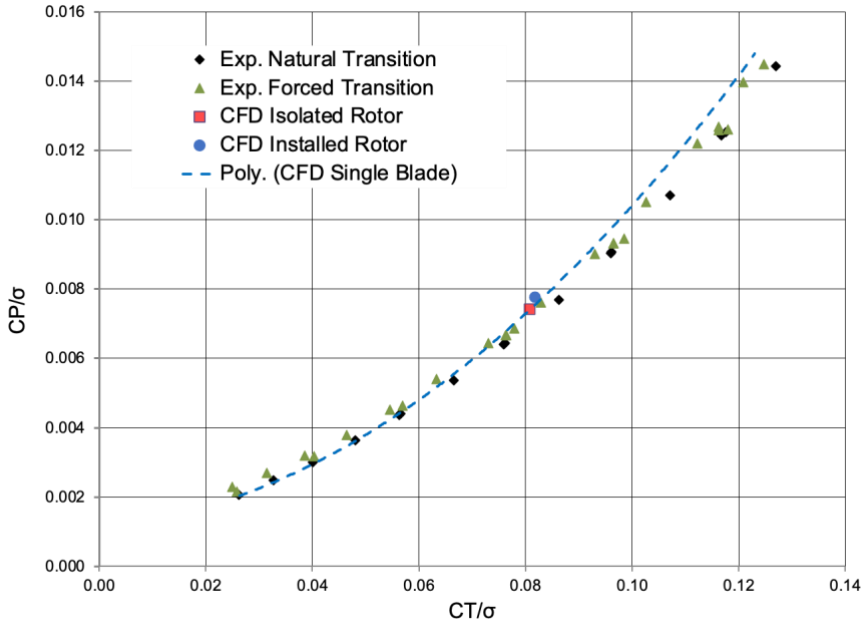

Figure 9. Comparison of Cp/s vs. Ct/s for isolated and installed rotors.

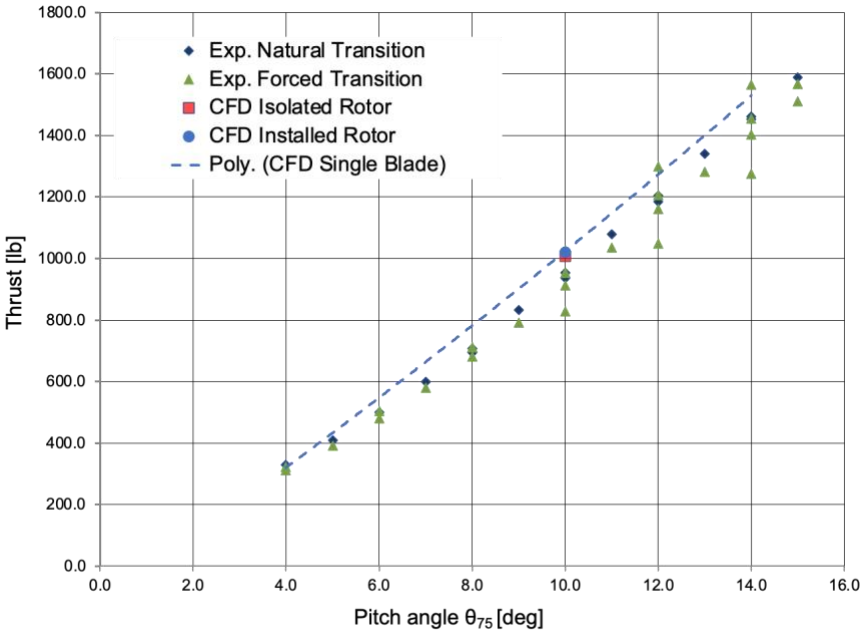

Figure 10. Comparison of rotor thrust vs. blade pitch angle for isolated and installed rotor.

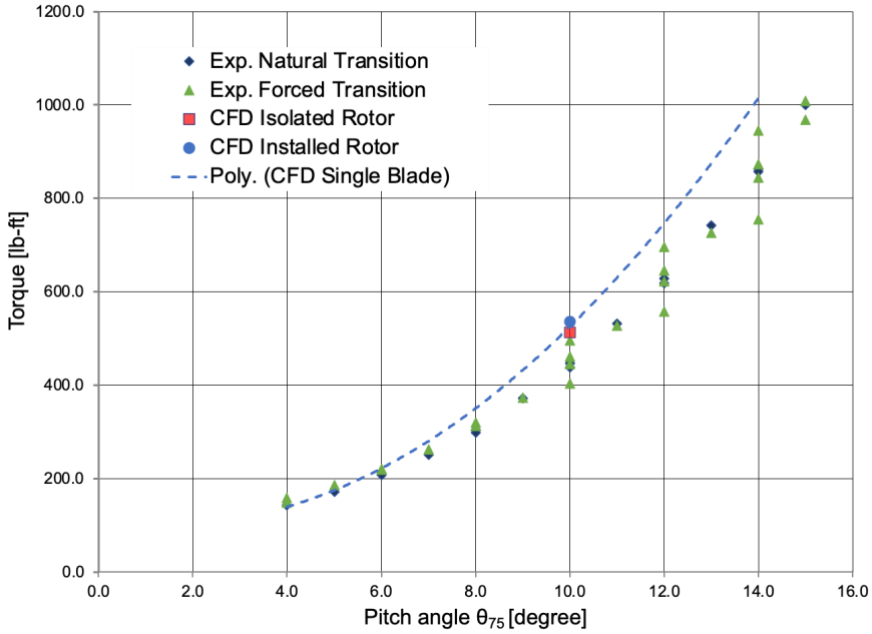

Figure 11. Comparison of rotor torque vs. blade pitch angle for isolated and installed rotor.

The rotor thermography image taken from the experiment [1] shows the boundary layer transition phenomenon observed on blade surfaces, as illustrated in Fig. 12 on the upper and lower surface at the selected blade pitch angle of 10°. The darker area denotes the laminar flow, while the lighter area denotes the turbulent flow. The intermittency parameters computed for isolated and installed rotors are shown in Fig. 13, where the blue color denotes the laminar flow and the red color denote the turbulent flow. The computations generally captured the trend of flow transitions on the HVAB rotor. However, the installed rotor shows reduced laminar flows on both upper and lower surfaces compared to the isolated rotor, due to the presence of the fuselage that triggers an earlier transition. To further improve the prediction of transitions, significantly refined surface grid resolutions are required on rotor blades [16].

Figure 14 illustrates the trailing tip vortices generated by the rotating blades in the installed rotor case, with similar wake vortex structures observed in the isolated rotor. Key observations from the simulations include the primary tip vortices as well as the secondary vortices in the rotor wake region. The primary vortices are helix-shaped trailing tip vortices generated by the rotating blades. The secondary vortices are developed in the normal direction of the primary vortex trajectory. These secondary vortices evolve and interact with the primary vortices, leading to the breakdown of the primary vortices in the downwash.

Heintz, et al. [17] conducted an experimental investigation on the rotor vortex system and observed the secondary vortices in their wind tunnel tests. They concluded the blade passing frequency as a primary trigger for the creation of secondary tip vortices and consequent vortex breakdown. However, there may be other factors that could influence the formation of secondary vortices as well as the vortex breakdown. Trailing tip vortices play a significant role in the rotor and airframe interactions or the blade and vortex interactions, which influences rotor system dynamics and noise generation. Further investigation into the secondary tip vortices and their interactions with primary tip vortices is needed to gain deeper insights into the rotor complex trailing vortex system.

These findings underscore the mutual influence of rotorcraft configuration and operational conditions on thrust, torque, and overall performance metrics. The presence of fuselage interactions, including ground effect, impacts rotor aerodynamic performance and contributes to the complexity of rotor wake structures.

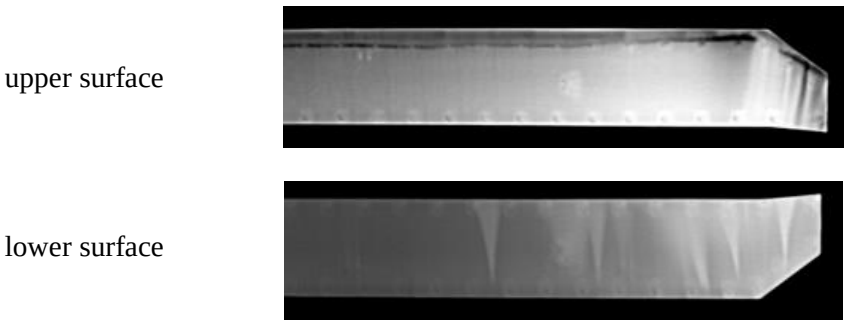

Figure 12. Measured flow transitions on HVAB rotor upper and lower surfaces, $\theta = 10°$.

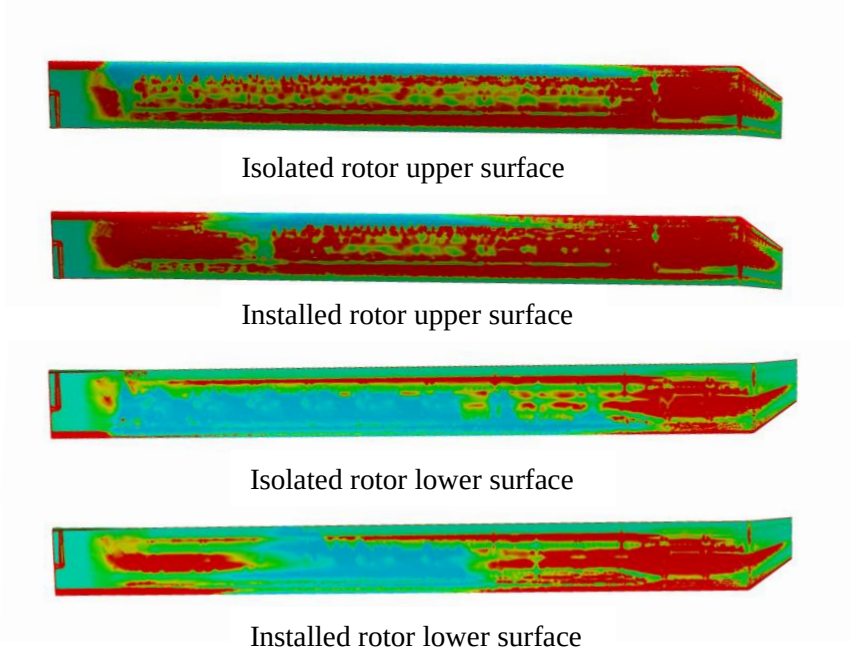

Figure 13. Computed flow transitions on HVAB rotor upper and lower surfaces, $\theta = 10°$.

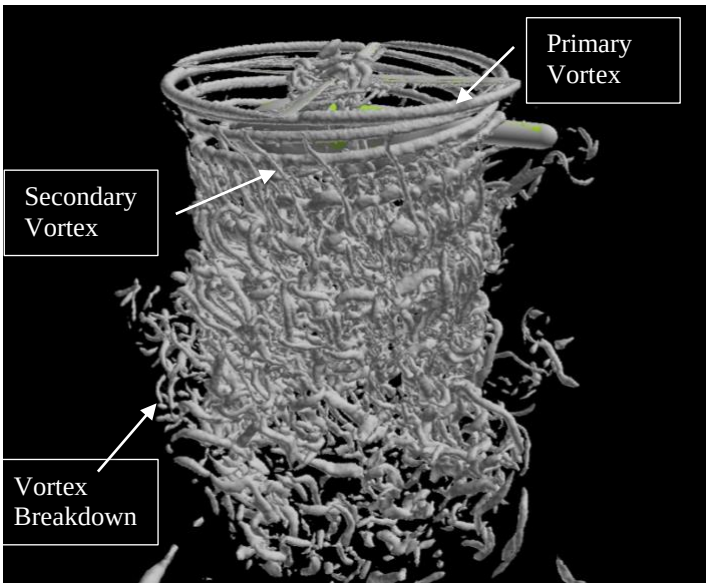

Figure 14. Trailing top vortices generated by rotating blades.

3.2 HVAB Rotor in Descent Flight

The second simulation conducted in this study is the HVAB installed rotor undergoing a descending flight to investigate its ground effect aerodynamics. A rotorcraft operating in hover is out of ground effect (OGE), while during descent flight is potentially in ground effect (IGE). The study of ground effect is of practical implications for helicopter safe operations, including challenges like brownout in desert environments or ground resonance during take-off and landing. Understanding rotor ground aerodynamics is crucial for enhancing safety and optimizing rotorcraft dynamics during ground operations.

Numerical simulations of an installed rotor during descent maneuver flight pose great challenges due to multi-body relative motions among the rotating rotor, the descending airframe, and the ground. To address these complexities, an overset grid technique is typically employed to facilitate data exchange among relative moving grids, as described in [18]. Moreover, maintaining a constant rotor gross weight during descent flight usually involves a rotor trimming process. This requires continuous adjustments to blade collective/cyclic settings while executing the descent maneuver, further complicating rotor blade motion dynamics.

As a preliminary step, the current study focuses on a numerical simulation for the HVAB rotor at a fixed blade pitch of 10° during descent maneuver. The techniques employed include mesh deformation and multibody relative grid motion as described earlier. The computational mesh for the HVAB installed rotor during descent flight is specifically generated due to the presence of the ground. The total mesh size is approximately 26.35 million points, which maintains the same surface resolution on the rotor and fuselage as in the previous hover cases. The ground is modeled as a viscous surface built with boundary layer mesh. There are three computational domains that involve relative motions: the rotor domain containing four rotating blades; the descending domain that contains the rotor and fuselage performing rigid descending motion; and the background domain undergoing the mesh deformation. Figure 15 shows two computational meshes for the installed rotor at its initial height (h = 2D) and final height (h = 1D), where D is the rotor diameter.

The simulation for the installed rotor during descent flight starts with the rotor positioned at an initial ground height, where the background flow has a uniform zero velocity. The installed rotor undergoes a descent motion at a prescribed descent speed as:

$$V = 6.9271 - 6.9271cos(\frac{\pi}{2}t) \tag{6}$$

This descending speed is designed to mimic a realistic flight operation, which allows the rotor to

descend 1.5 rotor diameters to its final height at half rotor diameter (h = 0.5D) within 2.4 seconds, or in 50 rotor revolutions. Due to the limitation of the mesh deformation method employed, the current simulation only allows the rotor to descend one rotor diameter (h = 1D), which took about 30 rotor revolutions. As illustrated in Fig. 15, which depicts the computational meshes before and after mesh deformation, mesh cells between the fuselage and the ground are visibly compressed to their maximum extent at the rotor final height (h = 1D), indicating that further mesh deformation is not feasible in this region.

Figure 16 illustrates the evolution of the trailing tip vortices at different instants during the descent flight of the HVAB rotor. The simulation begins with the rotor descending at the specified speed (6) until reaching its final height during the first 30 rotor revolutions. Subsequently, the simulation continues with the rotor hovering for another 20 rotor revolutions at this final height.

Initially, primary helical tip vortices start forming behind the rotor blades after several rotor revolutions. As the descent continues, secondary vortices become noticeable. These secondary vortices add complexity to the wake structure generated by the rotor. Over time, the secondary vortices interact with the primary vortices, leading to a breakdown and dissipation of the primary vortex structures under the influence of ground effect.

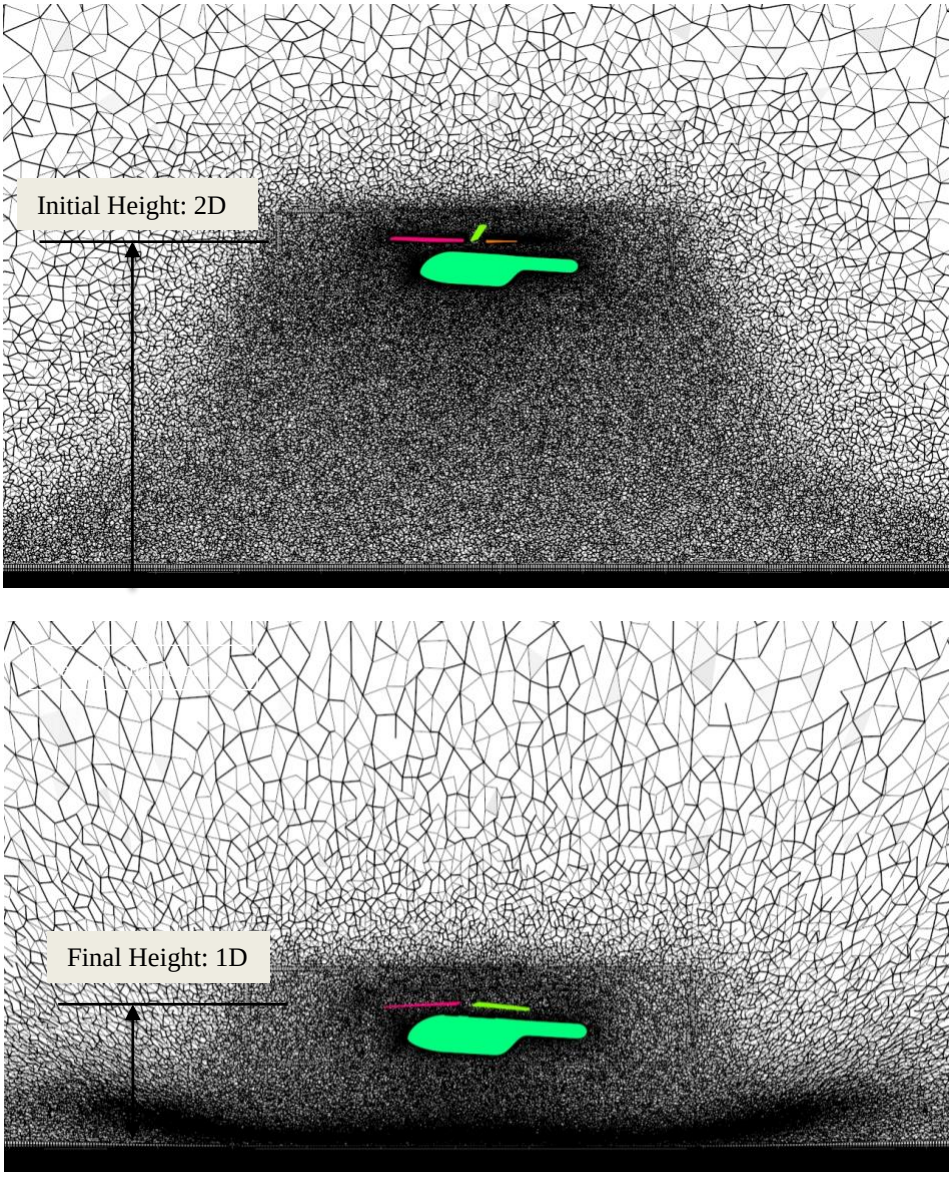

Figure 15. CFD meshes for installed HVAB rotor at initial and final heights of descent flight.

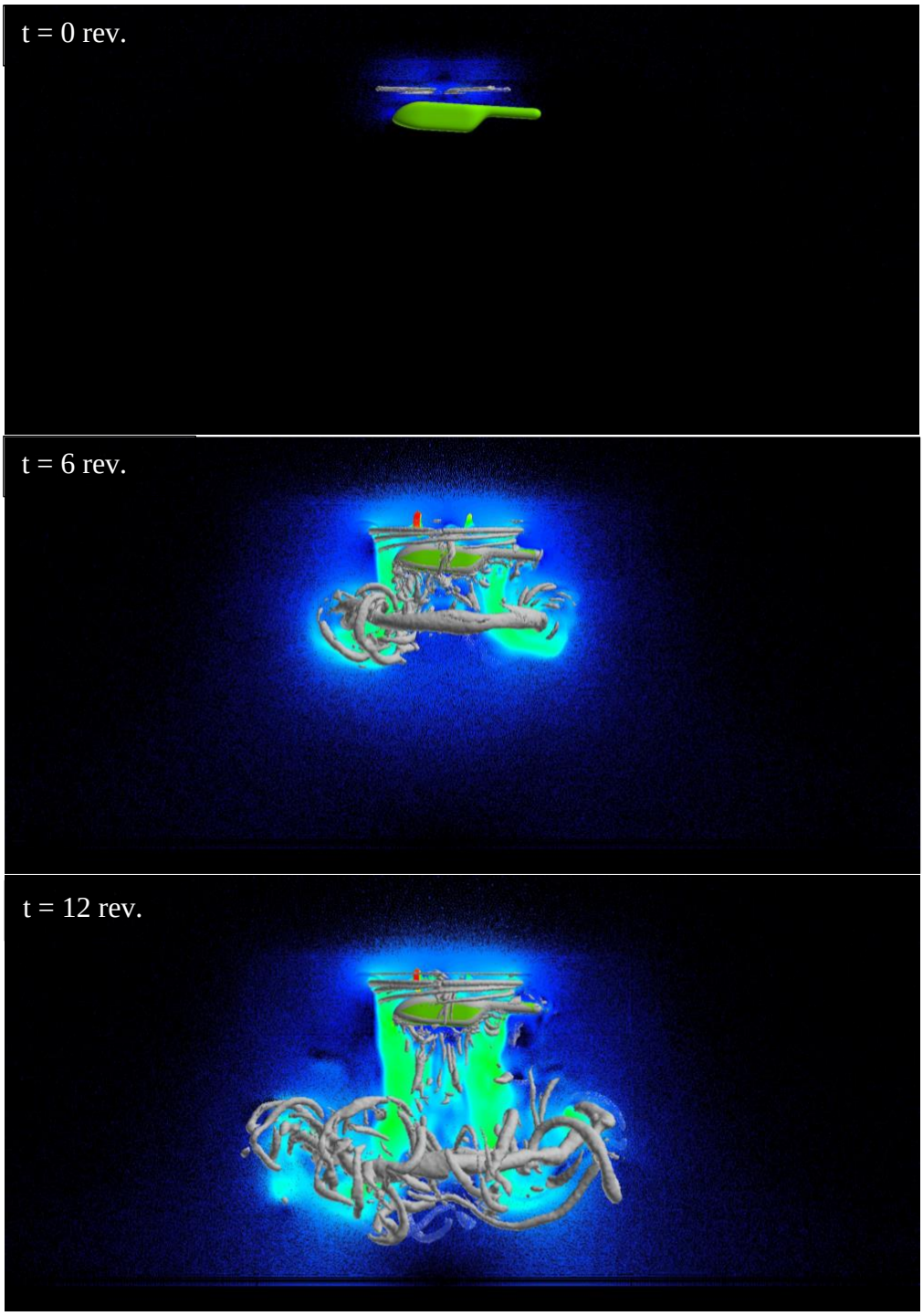
t = 0 rev.
t = 6 rev.
t = 12 rev.

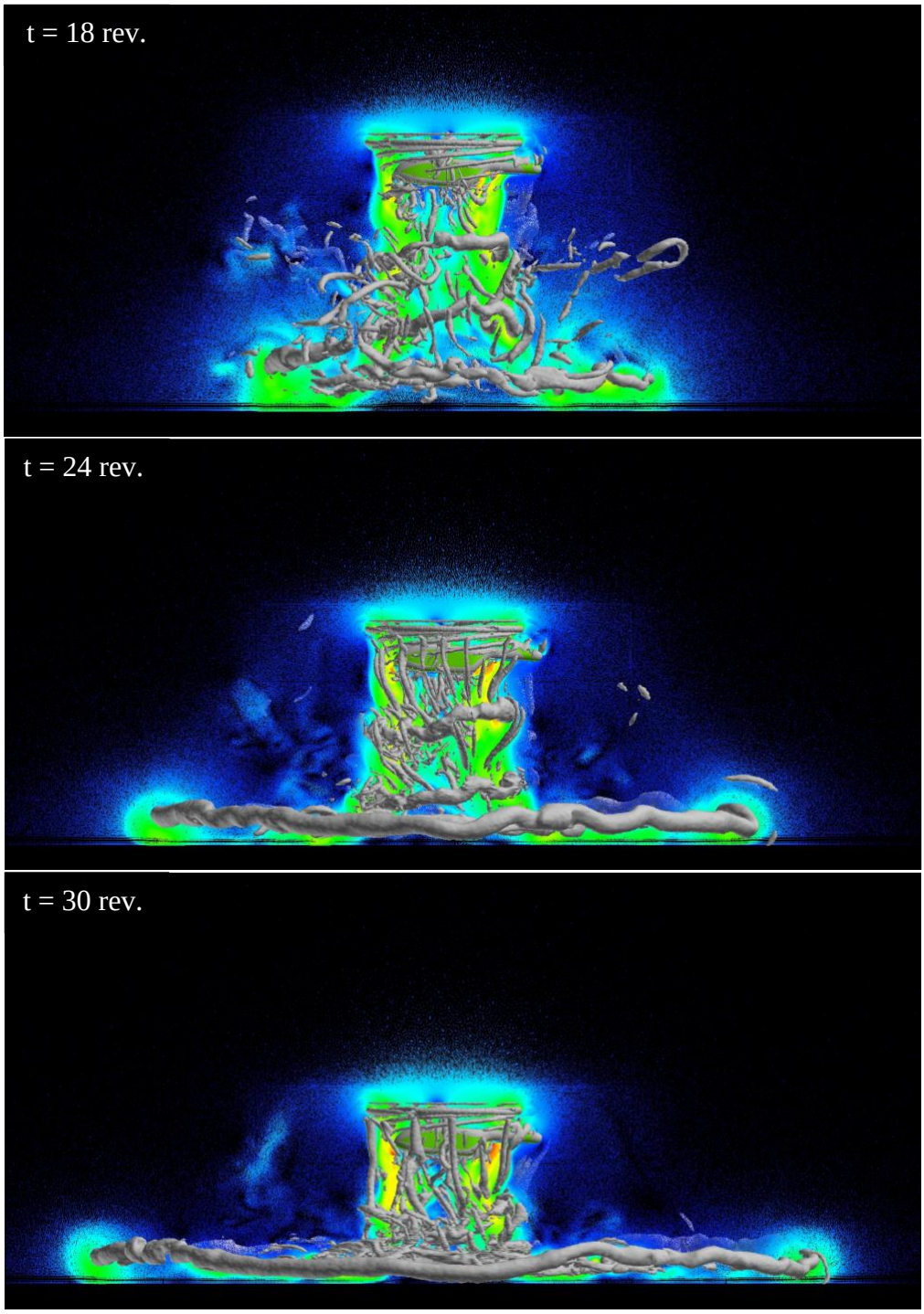

Figure 16: Predicted rotor tip vortices and velocity flow field for HVAB rotor at different moments in descent maneuver flight.

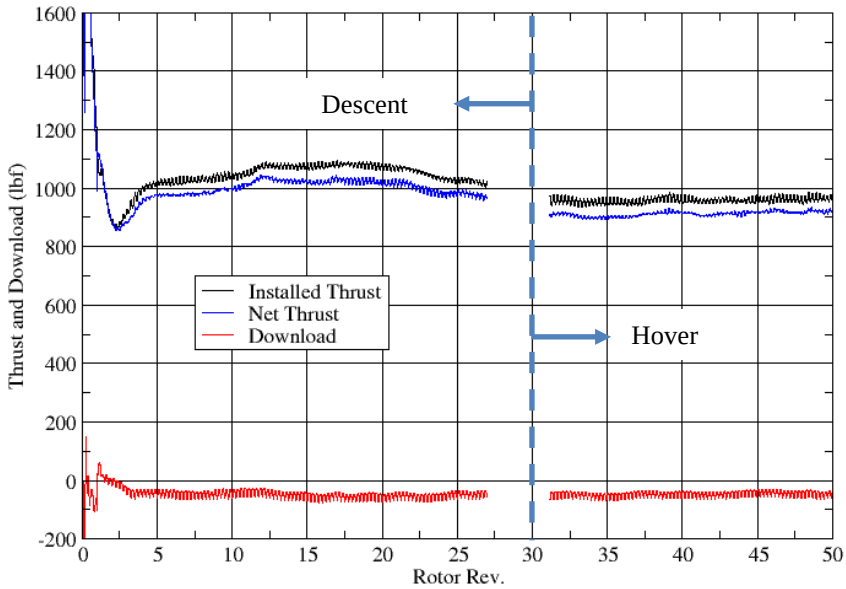

Figure 17: Predicted rotor installed thrust, net thrust, and download of the HVAB rotor in descent maneuver and hover flight.

Figure 17 presents the simulation results on the HVAB rotor's thrust characteristics during descent flight, showcasing rotor installed thrust, net thrust (gross weight), and fuselage download (negative lift). The rotor installed thrust represents thrust generated exclusively by the rotor blades, while net thrust (gross weight) is derived by subtracting the fuselage download from the installed thrust, indicating the effective thrust available to support the aircraft's weight.

Initially, following 3-4 rotor revolutions, rotor thrust increases as descent speed accelerates, peaking around 16 rotor revolutions. Subsequently, rotor thrust declines for the remainder of the descent. During the final 20 revolutions in hover, rotor thrust stabilizes at approximately 925-975 lbf.

These trends reflect the influence of descent speed, fixed blade pitch angle, and ground effect on rotor performance. The simulation underscores the need for rotor trim adjustments to maintain consistent net thrust (gross weight) during descent, an area warranting further investigation in rotorcraft simulations.

4 Conclusion and Future Work

This study presented computational simulations of a Hover Validation and Acoustic Baseline (HVAB) rotor operating in both hover and descent flight conditions. These simulations employed a hybrid RANS-LES approach, combining the Spalart-Allmaras (SA) turbulence model with the Wall-Adaptive Local Eddy viscosity (WALE) subgrid model to improve turbulence prediction accuracy. An entropy-based blending function was introduced to effectively distinguish between the near-wall RANS region and the off-wall LES region, ensuring accurate hybrid simulation results.

The computational framework utilized a new high-order compact Weighted Essentially Non-Oscillatory (WENO) scheme on unstructured grids, which significantly reduced numerical dissipation errors. Additionally, advanced unstructured grid techniques, such as multibody relative motion and mesh deformation, were employed to model the HVAB rotor's behavior during hover and descent modes. These techniques facilitated detailed and flexible rotor blade motions, accommodating the complex geometries and flow dynamics of rotorcraft in different flight conditions.

Future work will focus on investigating the rotor trimming process to maintain a constant gross weight during descent maneuvers. Additionally, analysis of the distributed sectional rotor thrust and torque along the rotor radius will be conducted to further understand the HVAB rotor's performance in

both hover and descent flight conditions. These efforts are crucial for optimizing the HVAB rotor's performance and enhancing its operational efficiency across diverse scenarios.

Acknowledgements

Graphic images shown in this work were created using FieldView, provided by Intelligent Light and TecPlot under University Partners Program. This support is gratefully acknowledged.

References

[1] Norman T. Status of NASA/Army Hover Test, AIAA SciTech Forum 2020.
[2] Sheng C. A preconditioned method for rotating flows at arbitrary Mach number. Modeling and Simulation in Engineering, Vol. 2011, January 2011.
[3] Sagaut P, Deck S, and Terracol M. Multiscale and multiresolution approaches in turbulence. Imperial College Press, 2006.
[4] Fröhlich J, von Terzi D. Hybrid les/rans methods for the simulation of turbulent flows. *Progress in Aerospace Sciences*, vol. 44, 2008, pp. 349–377.
[5] Spalart PR, Jou W-H, Strelets M, Allmaras SR. Comments on the feasibility of LES for wings, and on a hybrid RANS/LES approach. In: Proceedings of first AFOSR international conference on DNS/LES, Ruston, Louisiana, 1997.
[6] Egorov Y, and Menter F. Development and application of SST-SAS turbulence model in the DESIDER project. *Advances in Hybrid RANS-LES Modelling*, pp. 261–270.
[7] Spalart PR, Deck S, Shur M L, Squires KD, Strelets MK, and Travin A. A new version of detached-eddy simulation, resistant to ambiguous grid densities. *Theoretical and Computational Fluid Dynamics*, vol. 20, 2006, pp. 181–195.
[8] Sheng C, Zhao Q, Khan R. Assessment of hybrid RANS-LES methods for simulation of viscous flows. AIAA 2023 SciTech Conferences, AIAA 2023-1615, 23-27 January 2022, National Harbor, MD.
[9] Zhou L, Zhao R, Shi XP. An entropy-assisted shielding function in DDES formulation for the SST turbulence model. Special Issue, Entropy in Computational Fluid Dynamics, *Entropy* 2017, *19*(3), 93; https://doi.org/10.3390/e19030093.
[10] Zhong D, Sheng C. A new method towards high-order WENO schemes on structured and unstructured grids. *Computer & Fluids*, vol. 200, 2020, 104453.
[11] Sheng C, Allen C. Efficient mesh deformation using radial basis functions on unstructured meshes. *AIAA Journal*, Vol. 51, No. 3, pp. 707-720.
[12] Spalart PR, Allmaras S. A one-equation turbulence model for aerodynamic flows. 30th Aerospace Sciences Meeting and Exhibit, 1992.
[13] Nicoud F, Ducros F. Subgrid-scale stress modelling based on the square of the velocity gradient tensor, *Flow, Turbulence and Combustion*, Vol.62, 1999, pp. 183-200.
[14] Zhu J, Qiu J. A new type of finite volume WENO scheme for hypersonic conservation laws. *J Sci Comput*, 2017;73:1338-59.
[15] Sheng C, Ickes J, Wang J, Zhao Q. CFD/CSD coupled simulation for a helicopter rotor in forward and maneuvering flight. 31st Applied Aerodynamics Conference, AIAA-2013-2792, June 24-27, 2013, San Diego, CA.
[16] Zhao Q, Sheng C. Predictions of HVAB rotor in hover using hybrid RANS-LES methods II, 2022 AIAA SciTech Forum, 3-7 January 2022, San Diego, CA.
[17] Heintz A, Scheartz C, Wolf CH, and Raffel M. Influence of configurational parameters on the vortex system of a rotor in hover. 2024 AIAA SciTech Forum, 8-12 January 2024, Orlando, FL.
[18] Sitaraman J, Floros M, Wissink A, Potsdam M. Parallel domain connectivity algorithm for unsteady flow computations using overlapping and adaptive grids. *J. Compu Physics*, 229 (12), 2010, 4703-4723.